Modern Physics Letters B
Vol. 36, No. 7 (2022) 2150605 (19 pages)

DOI: 10.1142/S0217984921506053

Numerical investigations into supercavitating flows and hydrodynamic characteristics of a heaving hydrofoil

Yuchang Zhi

School of Aeronautics and Astronautics, Sun Yat-Sen University, Guangzhou 510275, China
zhiyuchang0129@163.com

Zhen Zhang

State Key Laboratory of Mechanical Behavior and System Safety of Traffic Engineering Structures, Shijiazhuang Tiedao University, Shijiazhuang 050043, China
zhangz@stdu.edu.cn

Renfang Huang*, Rundi Qiu† and Yiwei Wang‡

Key Laboratory for Mechanics in Fluid Solid Coupling Systems, Institute of Mechanics, Chinese Academy of Sciences, Beijing 100190, China
**hrenfang@imech.ac.cn*
†*qiurundi19@mails.ucas.edu.cn*
‡*wangyw@imech.ac.cn*

Received 30 August 2021
Revised 4 November 2021
Accepted 1 December 2021
Published 22 January 2022

This paper presents the effects of heaving motions on the hydrodynamic characteristics, supercavitating flow regimes and vortex structures for a two-dimensional (2D) supercavitating hydrofoil. The sinusoidal heaving motion of the supercavitating hydrofoil is realized by overset grid technology. The lift coefficient, drag coefficient, supercavitating flow regime and vortex structures around the supercavitating hydrofoil are analyzed and compared among different amplitudes of the heaving motion. The predicted cavities and the hydrodynamic characteristics are in good accordance with the experiments at a stationary state. The lift coefficient and drag coefficient of the heaving hydrofoil present a sinusoidal law, which is related to the effective angle of attack. The heaving motion would affect the cavity length and its thickness. The greater the heaving amplitude, the greater the difference in cavity pattern at different heaving positions. The cavity

*Corresponding author.

variation would affect the shear layer and thus change the vortex shedding characteristics, which are different from those at a stationary state.

Keywords: Supercavitation; supercavitating hydrofoil; heaving motion; overset grid; vortex structure.

1. Introduction

Cavitation is an unavoidable issue at the stage of the hydrofoil optimization design. On the one hand, partial cavitation would affect the hydrofoil hydrodynamics and lead to noise, vibration and possible structural failure.[1–5] On the other hand, in the supercavitating flow regime, since the density of the vapor phase is much lower than that of the liquid phase, the lift and resistance of the hydrofoil are significantly reduced, and consequently so are the vehicle's speed and stability.[6–9]

To date, lots of experiments have been conducted to investigate the supercavitating flow around a hydrofoil at different cavitation numbers in high-speed cavitation water tunnels.[10,11] Parkin conducted experiments on the supercavitating hydrofoils in which they visualized cavity shapes and determined the hydrodynamic performance at different cavitation numbers.[12,13] The lift coefficient and drag coefficient of the hydrofoils were consistent with the theoretical values under the same flow conditions (i.e. cavitation numbers). Kinnas *et al.*[14] measured the velocity flow field around a supercavitating hydrofoil in the high-speed water tunnel of the Massachusetts Institute of Technology by using a two-component laser Doppler velocimetry system (which was able to collect velocity components along the flow direction and the vertical direction at the same time). Their measurements of the velocity near the cavity surface verified the basic assumption that the pressure on the cavity was constant. Li *et al.* observed the supercavitating flow field in a high-speed cavitation water tunnel using a high-speed camera.[15] Their results indicated that the cavitating flow fields showed obvious differences in morphology at different cavitation numbers. These observations of the flow structures have shown that the supercavity around a hydrofoil is very stable and has a strong two-dimensional (2D) effect.[14] Therefore, the supercavitating flow regime can be simplified to a 2D supercavity.

With the rapid development of the computational fluid dynamics (CFD) calculation technology, much effort has been made to study the supercavitation by using the numerical simulations. Bonfiglio and Brizzolara[16] developed a highly accurate 2D supercavitation calculation method based on the RANS. The method was able to obtain the hydrodynamic performance and cavitating flow patterns for a supercavitating hydrofoil, and the simulated results were in good agreement with the experiments. Bonfiglio and Brizzolara[16] conducted experiments on a supercavitating hydrofoil in the free surface cavitation tunnel, and used these experiments to successfully validate the numerical simulations performed using a RANS solver and the Schnerr–Sauer cavitation model for the multiphase flow. Research shows that

the RANS method and Schnerr–Sauer cavitation model can well simulate the supercavitating flow.

Boudis *et al.*[17] studied the influence of non-sinusoidal motion on the propulsion performance of the hydrofoil and the vortex shedding process. The results show that the numerical simulation can obtain the main flow characteristics in the experiment. Zhang *et al.*[18–20] conducted a series of experiments and numerical simulations on the transient pitching Clark-Y hydrofoil. The results show that the numerical calculation results are in good agreement with the experimental measurements. The literature shows that the hydrodynamic performance and main flow characteristics of the hydrofoil in motion can be obtained through numerical simulation.

The literature review demonstrates that the supercavitation mechanism under stable conditions has been extensively studied, but we still have inadequate understandings of supercavitating flow features and hydrodynamic characteristics for a heaving hydrofoil. It is necessary to further shed light on the supercavitating flows around a heaving hydrofoil, since the marine vessel is usually operated under transient states, namely, swaying, surging, yawing, etc.[21–24] In this paper, the unsteady supercavitating flow is simulated under various heaving motions by using an overset grid approach. Section 1 describes the numerical approach, the simulation setup and its validation. Section 2 systematically explores the supercavitating vortical flow features and hydrodynamic characteristics for the hydrofoil under various heaving motion with different heaving amplitudes.

2. Numerical Approach

2.1. *Governing equations*

The continuity and momentum equations are the basic equations for solving cavitation flow

$$\frac{\partial \rho}{\partial t} + \frac{\partial(\rho u_i)}{\partial x_i} = 0, \tag{1}$$

$$\frac{\partial(\rho u_i)}{\partial t} + \frac{\partial(\rho u_i u_j)}{\partial x_j} = -\frac{\partial p}{\partial x_i} + \frac{\partial}{\partial x_j}\left(\mu \frac{\partial u_i}{\partial x_j}\right), \tag{2}$$

where ρ is the mixture density, u_i is the velocity component in the i direction, μ is the flow viscosity and p is the pressure. The viscosity and mixture density can be written as

$$\rho = \alpha_v \rho_v + (1 - \alpha_v)\rho_l, \tag{3}$$

$$\mu = \alpha_v \mu_v + (1 - \alpha_v)\mu_l, \tag{4}$$

where subscript l represents the liquid phase, subscript v represents the vapor phase and α is the volume fraction. The transport equation is expressed as

$$\frac{\partial(\rho_v \alpha_v)}{\partial t} + \frac{\partial(\rho_v \alpha_v u_j)}{\partial x_j} = \dot{m}, \tag{5}$$

where $\dot{m}$ is the mass transfer rate. And the Schnerr–Sauer[25,26] cavitation model is used

$$\dot{m} = -3\rho_v^3 \sqrt{n_0 \frac{4}{3}\pi \left[\alpha_v^2 - \alpha_v^3\left(1 - \frac{\rho_v}{\rho_l}\right)\right]} \operatorname{sign}(p_v - p) \sqrt{\frac{2}{3}\frac{|p_v - p|}{\rho_l}}, \tag{6}$$

where n_0 is the initial mean diameter of a bubble inside the fluid, the saturated vapor pressure is $p_v = 3540$ Pa.

In this paper, the standard k–ε turbulence model was adopted to closure the turbulent flow. The transport equations for the kinetic energy k and the turbulent dissipation rate ε are

$$\frac{\partial}{\partial t}(\rho k) + \nabla \cdot (\rho k \bar{u}) = \nabla \cdot \left[\left(\mu + \frac{\mu_t}{\sigma_k}\right)\nabla k\right] + P_k - \rho(\varepsilon - \varepsilon_0) + S_k, \tag{7}$$

$$\frac{\partial}{\partial t}(\rho \varepsilon) + \nabla \cdot (\rho \varepsilon \bar{u}) = \nabla \cdot \left[\left(\mu + \frac{\mu_t}{\sigma_\varepsilon}\right)\nabla \varepsilon\right] + \frac{1}{T_e} C_{\varepsilon 1} P_\varepsilon - C_{\varepsilon 2} f_2 \rho \left(\frac{\varepsilon}{T_e} - \frac{\varepsilon_0}{T_0}\right) + S_\varepsilon, \tag{8}$$

where f_2 is a damping function, σ_k, σ_ε, $C_{\varepsilon 1}$ and $C_{\varepsilon 2}$ are model coefficients, μ is the dynamic viscosity, $\bar{u}$ is the mean velocity, P_k and P_ε are production terms, S_k and S_ε are user-specified source terms and $T_e = k/\varepsilon$ is the large-eddy time scale. In the source terms, ε_0 is the ambient turbulence value.[27] T_0 is a specific time-scale

$$T_0 = \max\left(\frac{k_0}{\varepsilon_0}, C_t\sqrt{\frac{v}{\varepsilon_0}}\right), \tag{9}$$

where C_t is a model coefficient, ν is the kinematic viscosity.

2.2. *Simulation setup*

Figures 1 and 2 show the calculation model and the computational domain and boundary conditions, where the geometric model used a 2D flat hydrofoil,[12] c is the chord length ($c = 0.0442$ m) and α_0 is the angle of attack ($\alpha_0 = 7°$). The computational domain is divided into two regions, that is, the background region (in gray) and the overset region (in red). The hydrofoil is located in the overset grid region as shown in Fig. 2, which is used for heaving motion. The cavitation number σ is an important non-dimensional parameter,

$$\sigma = \frac{P_\infty - P_0}{0.5\rho U_0^2}, \tag{10}$$

where U_0 is the freestream velocity ($U_0 = 9.2$ m/s), P_∞ is the far field pressure, and P_0 is the saturated vapor pressure. The Reynolds number is defined as $Re = U_0 c/\nu = 4.52 \times 10^5$, where ν is the kinematic viscosity of the liquid.

A Cartesian grid is used for mesh generation, and a rectangular control volume is used to refine the grids around the hydrofoil. In order to ensure the $y$plus is less than 1, 20 layers are generated near the hydrofoil wall.

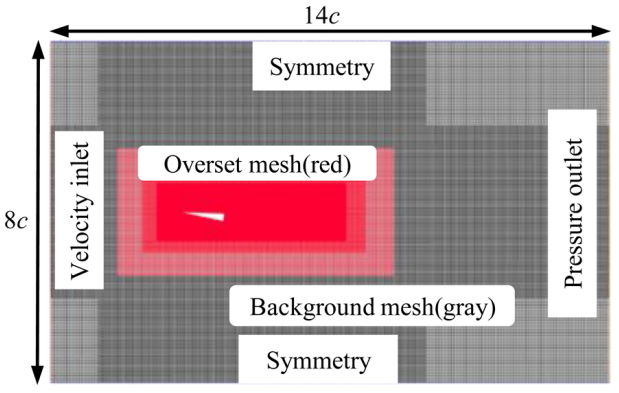

Fig. 1. (Color online) Computational domain and boundary conditions.

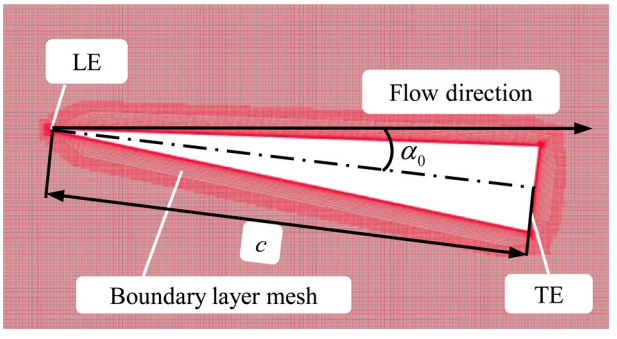

Fig. 2. (Color online) Overset grid details.

Vertical heaving motion of the supercavitating hydrofoil is realized by the autonomously defined Eq. (11) for the heaving distance $y(t)$,

$$y(t) = H_0 \sin(\omega t), \tag{11}$$

where H_0 is the amplitude of heaving motion and $\omega = 2\pi/T$ is the angular frequency, T is the variation cycle. Figure 3 is the schematic of the sinusoidal heaving motion of the hydrofoil, Fig. 3(a) shows main kinematic parameters of the heaving hydrofoil and waveform representation of the heaving hydrofoil position are illustrated in Fig. 3(b). $t = 0.00\ T$ is the mid-heaving location, and the hydrofoil moves upwards. $t = 0.25\ T$ is the maximum heaving location, and the hydrofoil starts to move downwards. $t = 0.50\ T$ is the mid-heaving locations, and the hydrofoil moves downwards. $t = 0.75\ T$ is the minimum heaving locations, and the hydrofoil starts to move upwards. During a heaving motion cycle, the hydrofoil first moves from the mid-heaving position ($t = 0.00\ T$) to the maximum heaving position ($t = 0.25\ T$), then from the maximum heaving position ($t = 0.25\ T$) to the minimum heaving position ($t = 0.75\ T$), and finally returns to the mid-heaving position.

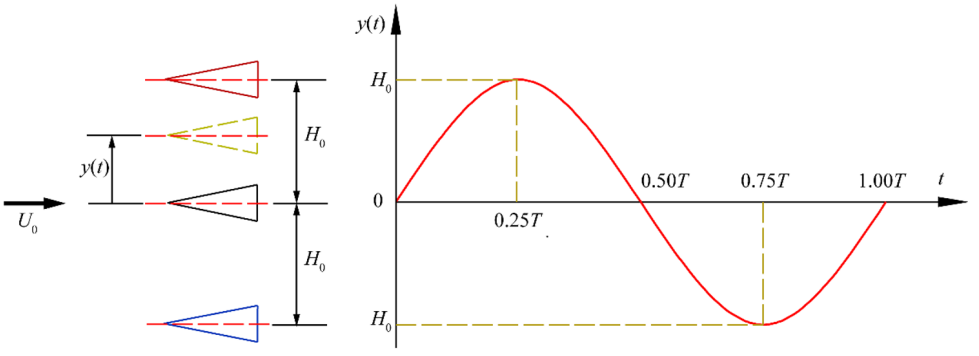

(a) Physical representation of hydrofoil motion (b) Waveform representation of hydrofoil position

Fig. 3. (Color online) Schematic of the heaving motion of the hydrofoil.

Table 1. Calculation conditions.

Condition	State	Re	σ	H_0/c	f_{Heaving} (Hz)
1	Stationary	4.52×10^5	0.566	—	—
			0.434		
			0.268		
			0.193		
2	Heaving	4.52×10^5	0.268	0.1	5
				0.25	
				0.5	

In order to analyze the effects of the heaving motion on the supercavitating flows around the hydrofoil, so the stationary state is simulated, and then the heaving amplitude (H_0) is discussed for the heaving motion, as shown in Table 1.

2.3. *Validation*

Mesh refinement helps to improve the calculation accuracy for a supercavitation. In order to perform the uncertainty analysis,[28] three sets of grids are created with the mesh refinement ratio r ($r = 2$) defined in Eq. (12),

$$r = \frac{N_{\text{fine}}}{N_{\text{coarse}}}, \tag{12}$$

where N is the cells number in the computational domain in the simulation. The time step is set to $\Delta t = T_{\text{ref}}/400 = 1.25 \times 10^{-5}$ s, where $T_{\text{ref}} = c/U_0$, as suggested by Zhang *et al.*[11] The lift coefficient C_L and drag coefficient C_D are calculated under the working conditions $\sigma = 0.268$ and $U_0 = 9.2$ m/s. These coefficients are defined as

$$C_L = \frac{L}{0.5\rho U_0^2 c}, \quad C_D = \frac{D}{0.5\rho U_0^2 c}. \tag{13}$$

Table 2. The hydrodynamic performance for different mesh grids.

	ID	Grid volume	Mean C_L	Error (%)	Mean C_D	Error (%)
Experiment[12]		—	0.4210	—	0.0863	—
Fine	$S1$	1160895	0.4116	2.233	0.0924	7.068
Medium	$S2$	601472	0.4132	1.853	0.09271	7.428
Coarse	$S3$	312880	0.4153	1.354	0.09318	7.972

Table 3. Parameters for uncertainty analysis.

	R_G	P_G	U_G
C_L	0.7619	0.7518	0.0093
C_D	0.6596	1.1413	0.0024

The hydrodynamic performance of the hydrofoil for different mesh grids are shown in Table 2. Taking the medium mesh as an example, the relative error compared with the experiments is 1.853% for the lift coefficient and 7.428% for the drag coefficient, which demonstrates that the present numerical approach meets the requirements for engineering applications.

Table 3 shows the parameters for the uncertainty analysis,[29] where P_G is the estimated order of accuracy, R_G is the grid convergence rate and U_G is the grid uncertainty. The grid convergence rate R_G is less than 1, so the calculated C_L and C_D converge monotonically with increasing the grid number. The results show that the grid uncertainties associated with C_L and C_D are less than 5%. Overall, the grid convergence validation indicated that the simulations are almost independent of the mesh.

Figure 4 shows the cavity shapes obtained by three sets of grid calculations and experiments at the condition of $\alpha = 7°$ and $\sigma = 0.268$. The cavity length predicted

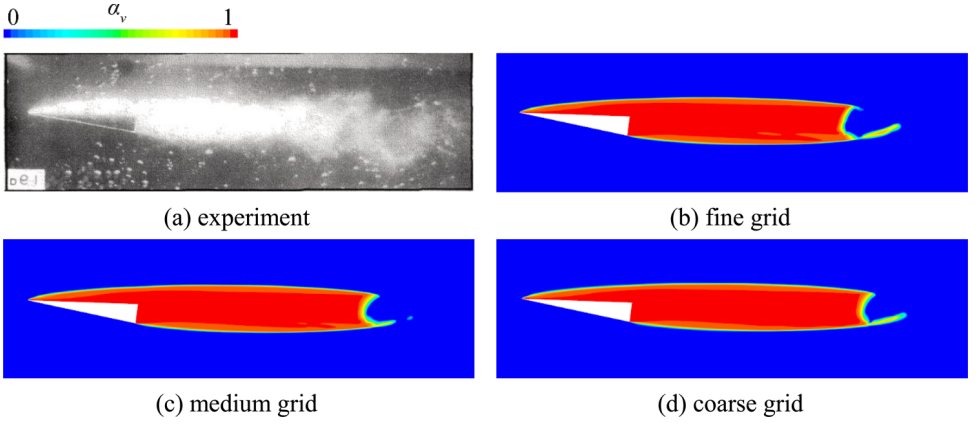

Fig. 4. (Color online) Comparisons between the simulations and experiments[12] at $\alpha = 7°$ and $\sigma = 0.268$.

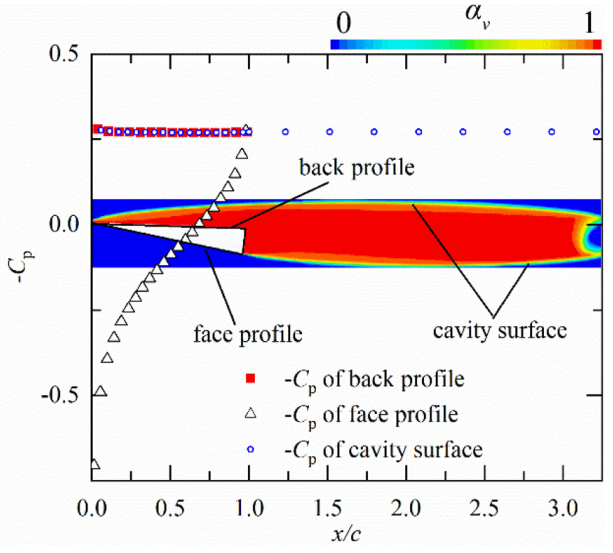

Fig. 5. (Color online) Pressure coefficient distributions on the hydrofoil surface and the cavity shape.

by the present numerical approach is basically consistent with the experiment. Figure 5 shows the pressure distribution on the hydrofoil surface and the cavity shape for the medium grid. The pressure coefficient C_p is defined as $C_p = (P - P_\infty)/\frac{1}{2}\rho U_0^2$, where P_∞ is the far field pressure and P is the static pressure at the point. In that case, a cavity would occur approximately where $\sigma = -C_p$, with σ defined as in Eq. (10), which is consistent with the experimental results.[14]

Based on the static hydrofoil simulation results, the same numerical parameters were used to verify the grid independence and time-step independence of the dynamic hydrofoil under $H_0 = 0.25c$, $T = 0.2$ s conditions. First, the study is carried out by using the same three grids as the stationary state. The time-step is set to $\Delta t = T_{\text{ref}}/400 = 1.25 \times 10^{-5}$ s in all cases. Figure 6 shows the changes in lift and drag coefficients during a heaving cycle. The results show that the results difference obtained by the three sets of grids is negligible. As shown in Table 4, the difference between the average lift and the average drag coefficient of the medium grid and the fine grid is 0.68% and 0.62%, respectively. Therefore, the medium mesh is considered fine enough to obtain reliable results.

Then, three different time steps of $T_{\text{ref}}/200$, $T_{\text{ref}}/400$ and $T_{\text{ref}}/800$ are used to study the time-step independence of the calculation results. These simulations used the medium grid. Figure 7 shows the changes in lift and drag coefficients during a heaving cycle, the lift and drag coefficient change curves are in good agreement. As shown in Table 4, the difference between the average lift and the average drag coefficient of the $T_{\text{ref}}/400$ and the $T_{\text{ref}}/800$ is 0.96% and 0.20%, respectively. Therefore, the time-step $T_{\text{ref}}/400$ and the medium grid are used in the following simulation.

Table 4. Grid and time-step independence study.

	Mesh	Time-step	Mean CL	Error	Mean CD	Error (%)
Grid independence	Fine	$T_{\text{ref}}/400$	0.40632	—	0.09128	—
	Medium		0.40357	0.68%	0.09071	0.62%
	Coarse		0.41186	1.36%	0.09242	1.25%
Time-step independence	Medium	$T_{\text{ref}}/800$	0.40750	—	0.09153	—
		$T_{\text{ref}}/400$	0.40357	0.96%	0.09171	0.20%
		$T_{\text{ref}}/200$	0.40142	1.49%	0.09026	1.39%

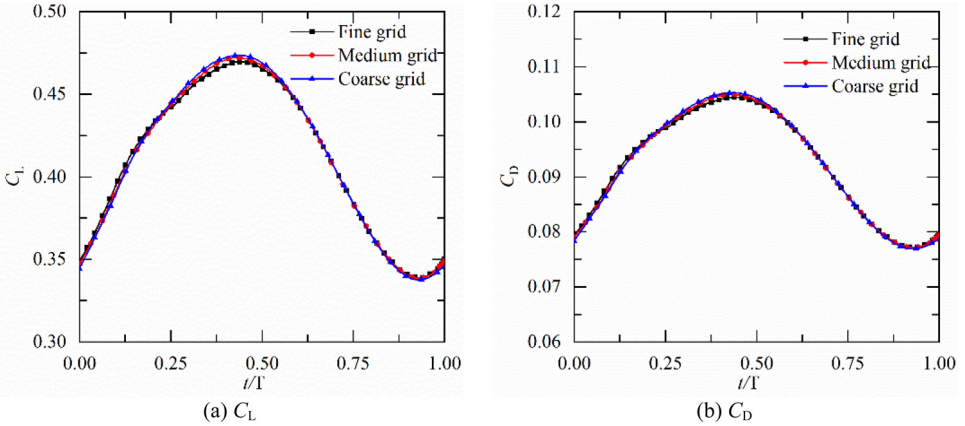

(a) C_L (b) C_D

Fig. 6. Grid independence study.

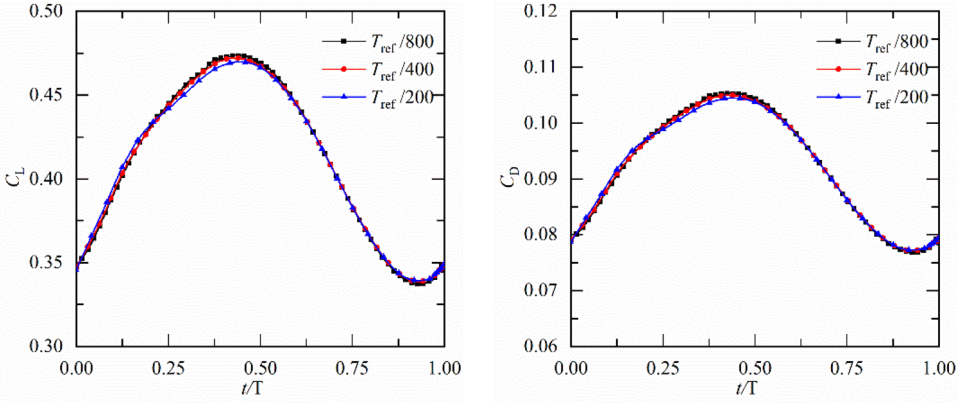

(a) C_L (b) C_D

Fig. 7. (Color online) Time-step independence study.

3. Results and Discussion

3.1. *Stationary state*

The hydrodynamic performance of the hydrofoil is calculated at various cavitation numbers and the experiments are taken for comparisons, as shown in Fig. 8. The calculated lift coefficient and drag coefficient are in good agreement with the experiments. As the cavitation number increases, the lift coefficient and drag coefficient gradually increase. The relative error of the lift coefficient with respect to experiments is generally below 5% and it becomes slightly larger for higher cavitation indices. The illustration of the box chart can be seen in Fig. 9. These charts demonstrate the fluctuation and average value of the C_L and C_D. At the same time, it can be seen from the box diagram that the greater the cavitation number, the

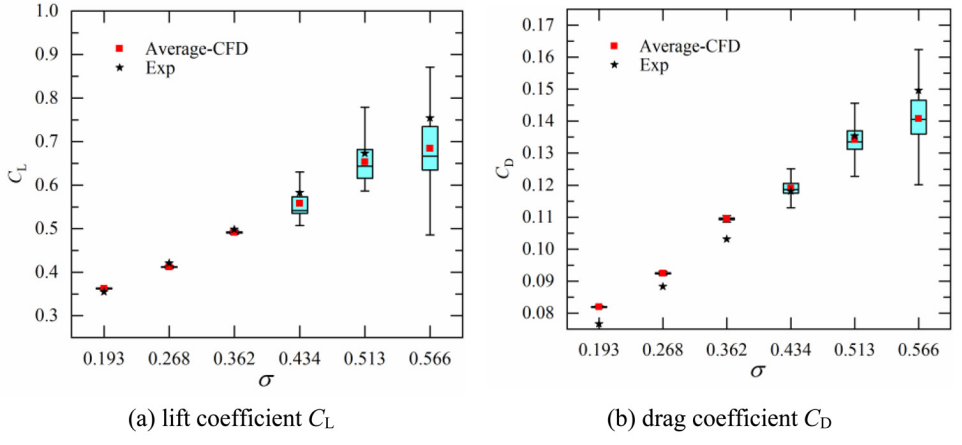

Fig. 8. (Color online) Comparisons of the C_L and C_D between the simulations and experiments in a stationary state.

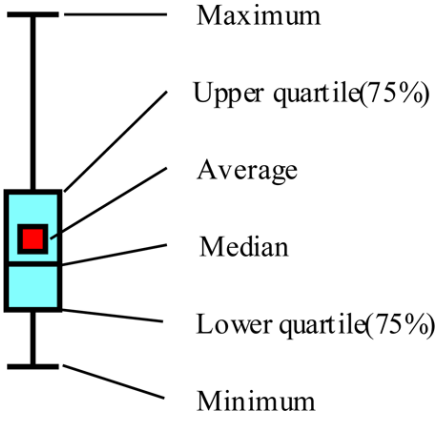

Fig. 9. (Color online) Statistic box plot.

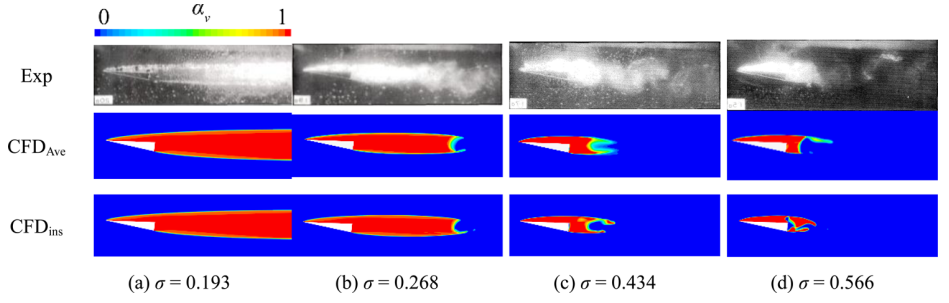

Fig. 10. (Color online) Comparisons of the supercavitating flow regimes between experiments[12] and simulations.

greater the fluctuation of the lift and drag coefficients. This proves the instability[30] of cavitating flow, which leads to the lift fluctuations. Generally, this phenomenon mainly occurs in the high-altitude number, the corresponding cavity length is relatively short, and the lift fluctuation corresponds to the cyclic vortex shedding, as shown in Figs. 10(c) and 10(d). Compared with the lift coefficient, the drag coefficient has a larger error with respect to the experiment.

Figure 10 compares the experimental and simulated supercavitating flow regimes under different cavitation numbers in a stationary state. It can be seen from the experimental results that the cavitation shape of the hydrofoil is mainly composed of a smooth and stable cavity and a cavitation vortex street mixed with air and water. Due to the limitations of URANS, it is difficult to capture the cavitation vortex street, so in this paper, we mainly used the length and thickness of the smooth and stable cavity to verify the accuracy of the calculation of the cavity shape. At the same time, compared with the instantaneous cavity shape and the average cavity shape ($t = 0.4$ s), it is found that they are basically the same in cavity length and thickness, and the average cavity is time-averaged between 0.3 s and 0.4 s. Furthermore, more refined turbulence model such as LES is preferred to resolve the turbulence production and dispersion more accurately. The flow regime is affected by the cavitation number and the supercavity separates from the hydrofoil leading edge, covering the entire hydrofoil suction surface, and then develops far from the hydrofoil trailing edge. As the cavitation number increases, the length and thickness of the supercavity decrease, and the supercavitating flow becomes unstable at a high cavitation number. As shown in Fig. 11(c), the supercavity is very short and unstable,[30] it is closured at about $0.5c$ aft of the trailing edge.

Figure 11 shows the vortex structures of the supercavitating wake for different cavitation numbers in a stationary state. Figure 12 is the schematic of the vortex structure in the supercavitating wake. It can be seen that the supercavity wake is divided into a near-wake region (A), a transition region (B) and a far-wake region (C). Region A is the supercavitation region, and the opposite vorticity is distributed up and down. In region B, the vortex at the tail of the supercavity begins to show flow separation. In region C, the vortices propagate downstream, forming

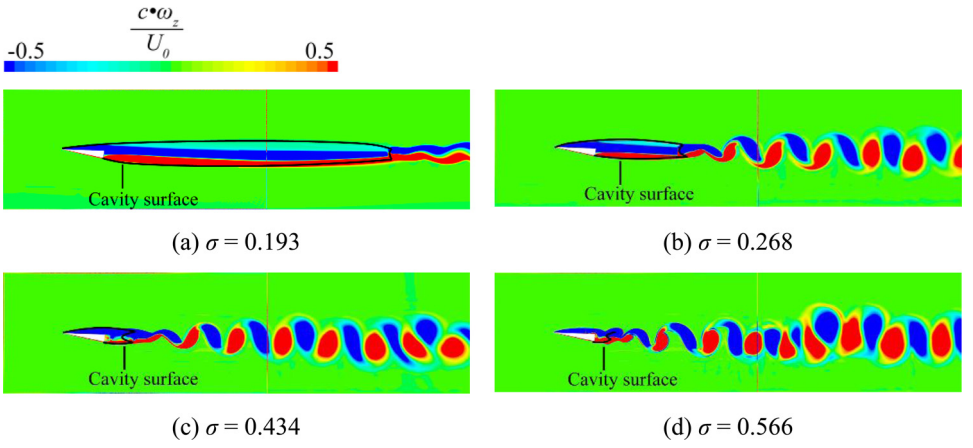

Fig. 11. (Color online) Instantaneous vorticity fields of the supercavitating wake in a stationary state.

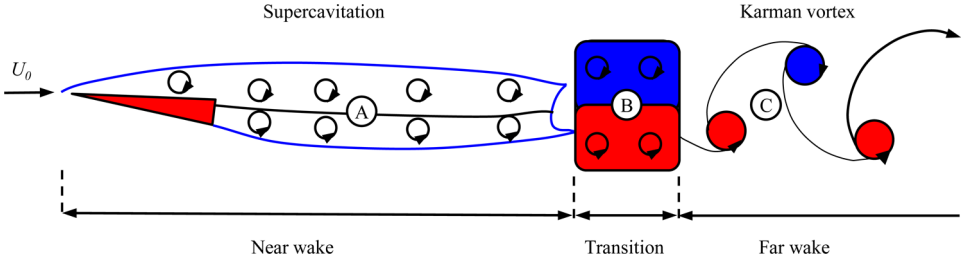

Fig. 12. (Color online) Schematic of the vortex structure in the supercavitating wake.

Kármán vortices, i.e. two spaced vortices with opposite directions of rotation. As shown in Figs. 10 and 11, the supercavity length decreases with increasing the cavitation number, and the vortex structure shedding mode changes at far-wake region (C). At the same time, it can be seen that with increasing cavitation number, the supercavity becomes unstable, which affects the stability of the wake flow.

3.2. *Effect of the heaving amplitude*

Figure 13 shows the supercavitating flow regime for different amplitudes of the heaving motion. $t = 0.00\ T$ is the mid-heaving location, and the hydrofoil moves upwards. $t = 0.25\ T$ is the maximum heaving location, and the hydrofoil starts to move downwards. $t = 0.50\ T$ is the mid-heaving locations, and the hydrofoil moves downwards. $t = 0.75\ T$ is the minimum heaving locations, and the hydrofoil starts to move upwards.

As for a typical motion cycle, from the minimum heaving location ($t = 0.75\ T$) to the maximum heaving location ($t = 0.25\ T$), the cavity length gradually becomes

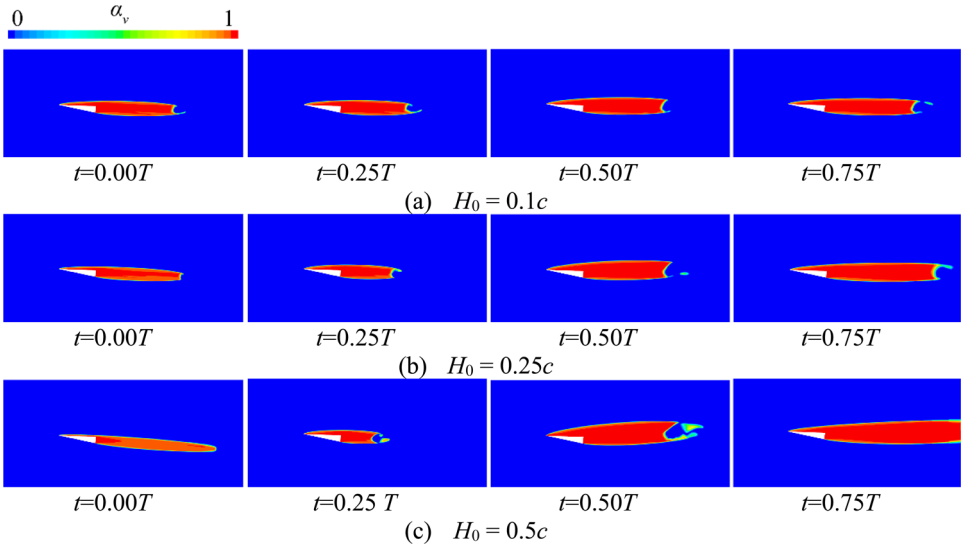

Fig. 13. (Color online) Supercavitating flow regime for different heaving amplitudes: (a) $H_0 = 0.1c$; (b) $H_0 = 0.25c$; (a) $H_0 = 0.5c$. The variation cycle of each heaving motion is $T = 0.2$ s.

shorter, and the cavity thickness is the thinnest at the mid-heaving location ($t = 0.00\ T$). During the movement of the hydrofoil from the maximum heaving location ($t = 0.25\ T$) to the minimum heaving location ($t = 0.75\ T$), the cavity length gradually becomes longer, and the cavity thickness is the thickest at the mid-heaving location ($t = 0.50\ T$). It is indicated that the cavity shifts to the opposite direction of the vertical heaving motion.

With the increase of the heaving amplitude, the cavity length becomes shorter at the maximum heaving location ($t = 0.25\ T$), it becomes longer at the minimum heaving location ($t = 0.75\ T$), the cavity thickness becomes thinner at $t = 0.00\ T$ and the cavity thickness becomes thicker at $t = 0.50\ T$. It is depicted that the instantaneous supercavitating flow regime is affected by the heaving amplitudes.

Figure 14 shows the vortex structure for different heaving amplitudes. For a specified heaving amplitude, the transient vortex structures in the near-wake region (A) are consistent with the cavitating region, and the instant vortex structures in the transition region (B) and far-wake region (C) are varied at different vertical heaving positions. Taking $H_0 = 0.5c$, for example, during one cycle, from the maximum heaving location ($t = 0.25\ T$) to the minimum heaving location ($t = 0.75\ T$), the cavity length gradually increases, the transition region (B) becomes further away from the hydrofoil tail with a longer shear layer, and thus the vortex shedding is suppressed to roll up from the shear layer with fewer counter-rotating vortex pairs. In contrast, from the minimum heaving location ($t = 0.75\ T$) to the maximum heaving location ($t = 0.25\ T$), the cavity length becomes shorter, so the shear layer near the liquid-vapor interface becomes shorter, causing the vortex shedding

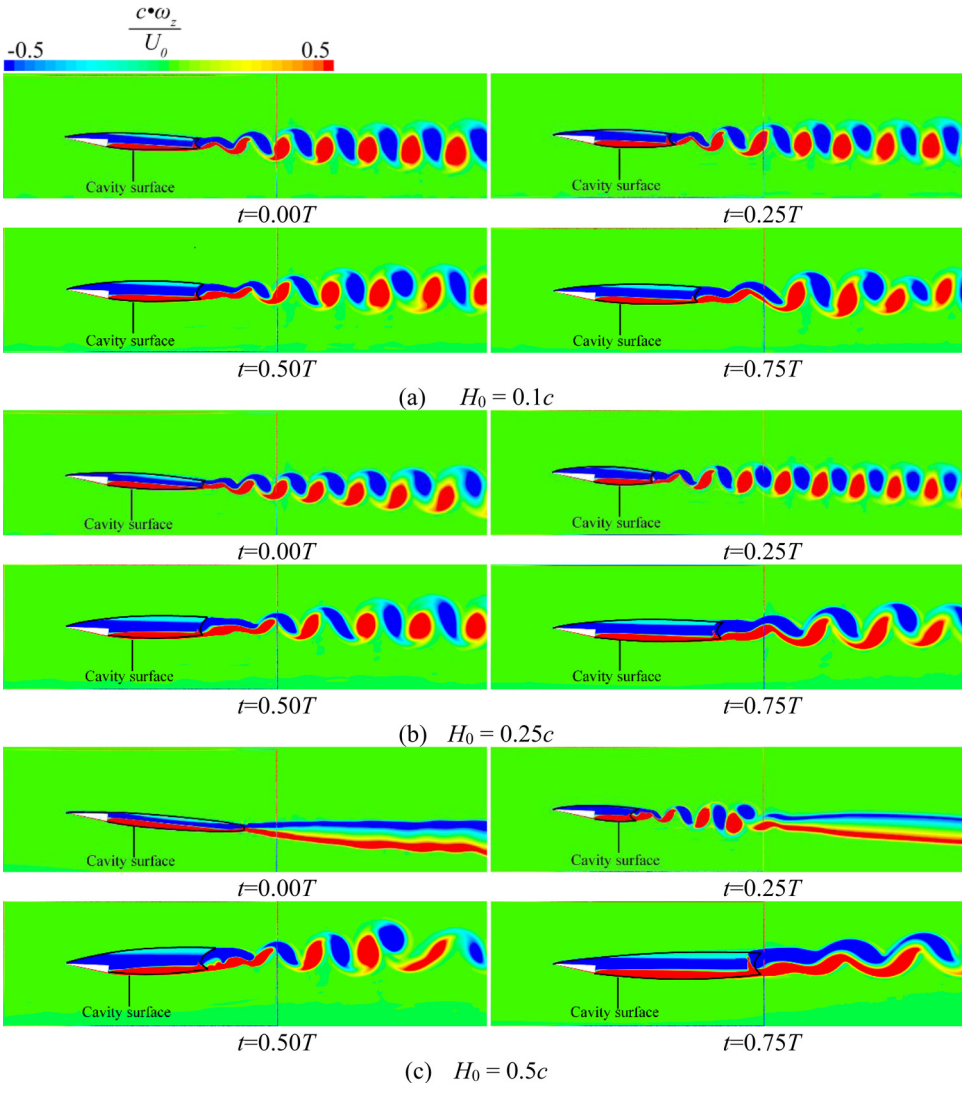

Fig. 14. (Color online) Instantaneous vorticity fields for different heaving amplitudes: (a) $H_0 = 0.1c$; (b) $H_0 = 0.25c$; (a) $H_0 = 0.5c$. The variation cycle of each heaving motion is $T = 0.2$ s.

is enhanced with more counter-rotating vortex pairs. It is depicted that the vortex structures shift to the opposite direction of the vertical heaving motion.

The vortex structure is suppressed or enhanced at different positions because the cavity length and thickness change with the heaving amplitude increases. For small heaving amplitude, the vortex shedding patterns are similar to those at the stationary state and the Karman vortex street is basically on the same horizontal line when it drifts into the wake. As the heaving amplitude increases, the vortex shedding pattern becomes more complicated at different heaving positions and the

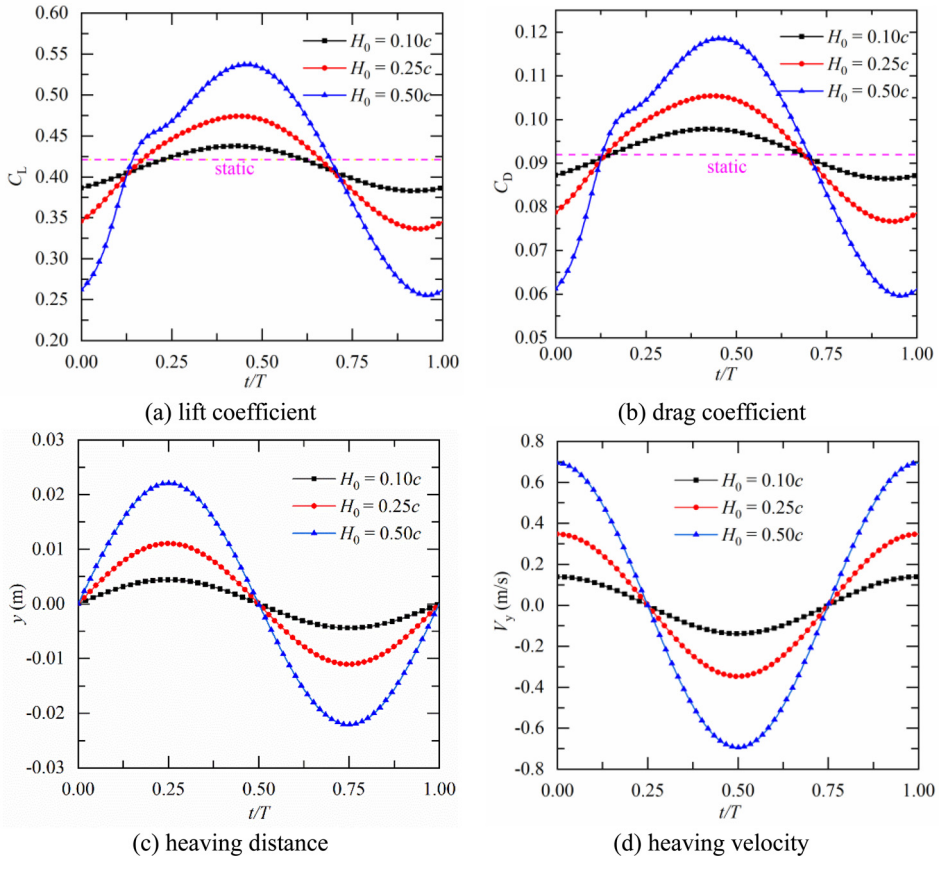

Fig. 15. (Color online) Time histories of (a) lift coefficient C_L, (b) drag coefficient C_D, (c) heaving distance and (d) heaving velocity. The variation cycle of each heaving motion is $T = 0.2$ s.

Karman vortex street shifts to the opposite direction of the vertical heaving motion. The vortex structure shedding pattern is the same at $t = 0.50\ T$, and the vortex structure shedding mode is greatly affected by the amplitude at $t = 0.00\ T$, $t = 0.25\ T$ and $t = 0.75\ T$.

Figure 15 shows the time histories of the lift coefficient C_L, drag coefficient C_D, heaving distance and vertical heaving velocity at different heaving amplitudes. Both the lift coefficient and the drag coefficient present sinusoidal variation trend which correspond to the heaving motion. It is noted that both the lift and the drag lag the heaving motion by $0.25\ T$, indicating that the vertical heaving position is maximum at $t = 0.25\ T$ and minimum at $t = 0.75\ T$ while the lift and drag would arrive at the peak at $t = 0.50\ T$ and at the trough at $t = 1.0\ T$. With increasing the heaving amplitude from $H_0 = 0.1c$ to $H_0 = 0.5c$, the maximum value of the lift coefficient increases from 0.44 to 0.54, and the maximum value of the drag coefficient increases from 0.098 to 0.119, demonstrating that the increase in the

heaving amplitude would cause the increase in the lift and drag of the hydrofoil while it does not make sense to the variation cycle.

3.3. *Relationship between hydrodynamic performance and the heaving motion*

To further study the influence of heaving motion on hydrofoil hydrodynamics, the relationship between hydrodynamic performance and heaving motion is presented, as shown in Fig. 16. When the hydrofoil heaves, the effective angle of attack α_{eff} is the sum of the induced angle caused by heaving motion and the angle of attack (α_0) with respect to the free stream, which is defined in Eq. (14). It is indicated that α_{eff} is mainly related to the amplitude H_0, the angular frequency ω ($\omega = 2\pi/T$, where T is the variation cycle), the flow velocity U_0 and the angle of attack α_0

$$\alpha_{\text{eff}} = -\arctan\left(\frac{\dot{y}}{U_0}\right) + \alpha_0 = -\arctan\left[\frac{H_0\omega\cos(\omega t)}{U_0}\right] + \alpha_0. \tag{14}$$

Figure 16 shows the relationship between hydrodynamic performance and heaving motion ($T = 0.2$ s). The effective angle of attack (α_{eff}) is the smallest at the mid-heaving locations ($t = 0.00\ T$) and the largest at the mid-heaving locations ($t = 0.50\ T$), which is equal to the angle of attack (α_0) at the maximum heaving location ($t = 0.25\ T$) and the minimum heaving location ($t = 0.75\ T$). In a typical heaving cycle, the α_{eff} increases from the minimum to the maximum (from $t = 0.00\ T$ to $t = 0.50\ T$), and then from the maximum to the minimum (from $t = 0.50\ T$ to $t = 1.00\ T$). It can be seen from Fig. 16 that the C_L and C_D of the hydrofoil are related to the α_{eff}. In a typical heaving cycle, the C_L and C_D of the hydrofoil increase with the increase of the α_{eff} (from $t = 0.00\ T$ to $t = 0.50\ T$) and decrease with the decrease of the α_{eff} (from $t = 0.50\ T$ to $t = 1.00\ T$).

According to Eq. (14), the heaving amplitude H_0 has a great effect on the α_{eff}. When the heaving amplitude increases, the α_{eff} will increase, so the C_L and C_D of the hydrofoil will also increase, as shown in Fig. 13. At the same time, it affects the cavitating flow field around the hydrofoil at different positions, as described in Sec. 3.2. Since the effective angle of attack of the hydrofoil is always changing, the flow field distribution around the hydrofoil is changed, and then the surface pressure distribution of the hydrofoil is changed, so the lift and drag coefficient of the hydrofoil changes with the effective angle of attack change. When the heaving amplitude of the hydrofoil is small, the flow field around the hydrofoil changes smoothly, so the curve of the lift and drag coefficient of the hydrofoil is relatively smooth. As the heaving amplitude of the hydrofoil increases, the flow field around the hydrofoil changes drastically, so the curve of the lift and drag coefficient of the hydrofoil also changes more drastically.

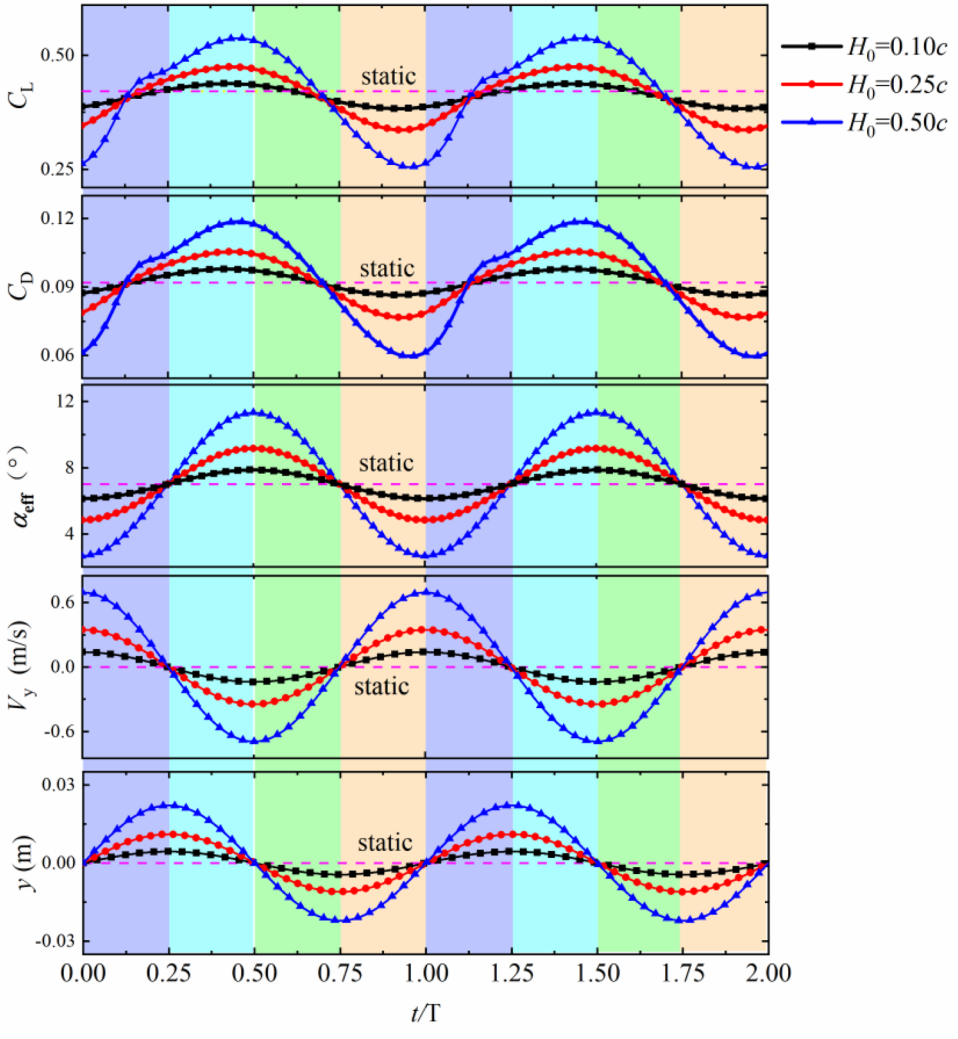

Fig. 16. (Color online) The relationship between hydrodynamic performance and heaving motion ($T = 0.2$ s).

4. Conclusions

In this paper, the overset grid approach is used to numerically simulate the heaving motion of the supercavitating hydrofoil. The hydrodynamic performance, supercavitating flow regime and vortex structures are investigated. The results are concluded as follows:

(1) With increasing cavitation number, the supercavity length and the supercavity thickness decrease, and the cavitating flow becomes unstable at high cavitation numbers. The vortex structure shedding mode is related to the cavity flow

pattern. The wake flow is divided into a near-wake region (A), a transition region (B) and a far-wake region (C).

(2) The lift coefficient C_L and drag coefficient C_D are connected with the current hydrofoil position and the effective angle of attack α_{eff}, which depends on the heaving amplitude H_0. When the heaving amplitude increases, the α_{eff} will increase, and thus the lift coefficient and drag coefficient will also increase.

(3) The length and thickness of the cavity vary at different heaving positions, which are related to the α_{eff}. When the heaving amplitude increases, the cavity pattern becomes more complicated, and the cavity shifts to the opposite direction of the vertical heaving motion.

(4) The vortex structure is correlated with the cavity pattern, since the cavity length and thickness will change the distribution of the shear layer. The vortex shedding process is greatly affected by the heaving amplitude. With a larger amplitude of heaving motion, the vortex shedding characteristics are more complicated at different hydrofoil heaving positions and the vortex structure moves further in the opposite direction of the vertical heaving motion.

Acknowledgments

The authors would like to gratefully acknowledge the National Natural Science Foundation of China (Grant Nos. 52006232, 11772340 and 12122214), the Youth Innovation Promotion Association CAS (Y201906) and the Science and Technology on Water Jet Propulsion Laboratory (Grant No. 6142223190101).

References

1. M. Dular, R. Bachert, B. Stoffel and B. Širok, *Eur. J. Mech. B Fluid* **24** (2005) 522.
2. X. Luo, B. Ji, X. Peng, H. Xu and M. Nishi, *J. Fluid Eng.* **134** (2012) 041202.
3. L. Zhou and Z. Wang, *J. Fluid Eng.* **130** (2008) 011302.
4. R. F. Huang, T. Z. Du, Y. W. Wang and C. G. Huang, *J. Hydrodyn.* **32** (2020) 865.
5. X. W. Luo, R. F. Huang and B. Ji, *Mod. Phys. Lett. B* **30** (2016) 1550262.
6. C. Xu and B. C. Khoo, *Phys. Fluids* **32** (2020) 123307.
7. R. F. Huang, S. Y. Shao, R. E. Arndt, X. W. Luo, Y. W. Wang and J. R. Hong, *J. Fluid Eng.* **142** (2020).
8. Y. Savchenko, http://resolver. caltech. edu/cav2001:lecture.003.
9. A. Acosta, *Annu. Rev. Fluid Mech.* **5** (1973) 161.
10. X. B. Li, G. Y. Wang, M. D. Zhang and W. Shyy, *Int. J. Therm. Sci.* **47** (2008) 1263.
11. M. J. Zhang, H. Chen, Q. Wu, X. B. Li, L. Xiang and G. Y. Wang, *Ocean Eng.* **173** (2019) 298.
12. B. R. Parkin, *Experiments on Circular Arc and Flat Plate Hydrofoils in Noncavitating and Full Cavity Flows* (1956).
13. P. Leehey and T. Stellinger, *J. Fluid Eng.* **97** (1975) 453.
14. S. A. Kinnas and C. Mazel, *J. Fluid Eng.* **115** (1993) 760.
15. X.-B. Li, N. Li and G.-Y. Wang, *J. Hydrodyn.* **28** (2016) 757.
16. L. Bonfiglio and S. Brizzolara, *Nav. Eng. J.* **128** (2016) 47.
17. A. Boudis, A.-C. Bayeul-Laine, A. Benzaoui, H. Oualli, O. Guerri and O. Coutier-Delgosha, *J. Fluid Eng.* **141** (2019).

18. M. Zhang, Q. Wu, G. Wang, B. Huang, X. Fu and J. Chen, *Renew. Energy* **150** (2020) 412.
19. M. Zhang, B. Huang, Q. Wu, M. Zhang and G. Wang, *Renew. Energy* **161** (2020) 1276.
20. M. Zhang, B. Huang, Z. Qian, T. Liu, Q. Wu, H. Zhang and G. Wang, *Int. J. Multiph. Flow* **132** (2020) 103408.
21. S. X. Huang, J. L. Jiao and C. H. Chen, *J. Mar. Sci. Technol.* (2021) 1.
22. Y. Sun, S. Zhong, T. Zhou, X. Huang and X. Zhang, *J. Sound Vib.* **472** (2020) 115209.
23. M. J. Zhang, Q. Wu, G. Y. Wang, B. Huang, X. Y. Fu and J. Chen, *Renew. Energy* **150** (2020) 412.
24. M. J. Zhang, B. Huang, Q. Wu, M. D. Zhang and G. Y. Wang, *Renew. Energy* **161** (2020) 1276.
25. B. Ji, X. Luo, R. E. Arndt, X. X. Peng and Y. L. Wu, *Int. J. Multiph. Flow* **68** (2015) 121.
26. B. Ji, Y. Long, X. P. Long, Z. D. Qian and J. J. Zhou, *J. Hydrodyn. Ser. B* **29** (2017) 27.
27. P. R. Spalart and C. L. Rumsey, *AIAA J.* **45** (2007) 2544.
28. H. Guo, J. Hu, C. Y. Guo, W. P. Zhang and J. F. Lin, *Phys. Fluids* **32** (2020) 095113.
29. P. J. Roache, *Annu. Rev. Fluid Mech.* **29** (1997) 123.
30. A. J. Acosta, *A Note on Partial Cavitation of Flat Plate Hydrofoils* (1955).